Quantum Tomography of Entangled Spin-Multiphoton States

Dan Cogan, Giora Peniakov, Oded Kenneth, Yaroslav Don, and David Gershoni[*]

The Physics Department and the Solid State Institute, Technion—Israel Institute of Technology, Haifa 3200003, Israel

We present a method for quantum tomography of multiqubit states. We apply the method to spin-multiphoton states, which we generate using a quantum dot based device. Periodic excitation of a quantum dot confined spin deterministically generates strings of entangled photons in a cluster state, threefold faster than previously demonstrated. Our tomography method uses time-resolved polarization-sensitive multiphoton correlation measurements to measure both the polarization of the confined spin and that of the emitted photons. We develop an edge-sensitive gradient-descent algorithm and apply it to the acquired data to map the periodic physical process that generates the cluster state. We utilize our tomographic method to optimize our quantum dot based device and show that the enhanced generation rate increases the entanglement robustness of the generated multiqubit state.

I. INTRODUCTION

Measurement-based quantum protocols are very promising for quantum computation in general [1–3] and for quantum communication in particular [4–7]. The use of multipartite entangled states, called graph states [8,9], enables quantum computation by single-qubit measurements and rapid classical feedforward, depending on the measurement outcome [2]. For quantum communication, graph states of photons are particularly attractive [10–14], since they provide redundancy against photon loss and compensation for the finite efficiency of quantum gates. Moreover, since the quantum information is contained in the graph state, they eliminate the need to communicate within the coherence time of the local nodes [7]. Graph states are therefore considered for efficient distribution of entanglement between remote nodes [15] as well as for quantum repeaters [5,6]. The development of devices capable of deterministically producing high-quality photonic graph states at a fast rate is, therefore, a scientific and technological challenge of the utmost importance [16–19].

The technological quest for the generation of photonic graph states, which are required for building scalable quantum network architectures, has led to a variety of further studies. Of particular importance and relevance to this work is the Lindner and Rudolph proposal [20] for generating a one-dimensional (1D) cluster state of entangled photons using semiconductor quantum dots (QDs). The scheme uses a single confined electronic spin in a coherent superposition of its two eigenstates. The spin precesses

in a magnetic field while driven by a temporal sequence of resonant laser pulses, every quarter of a precession period. Upon excitation of the QD spin, a single photon is deterministically emitted and the photon polarization is entangled with the polarization of the QD spin. This timed excitation repeats itself indefinitely, thus generating a long 1D cluster of entangled photons.

QD confined-spin–single-photon entanglement has been demonstrated for the exciton [21]. Since the two exciton spin states form an optical Λ system with a nondegenerate biexciton level, the radiative recombination of a biexciton results in a maximally entangled exciton-photon pair [22]. This unique feature of the exciton spin qubit also allows us to fully control its state, using a single short optical pulse (holonomic single-qubit gate [23]). In contrast, the QD confined electron and hole spin states form optical Π systems with the two levels of their excited trions. Therefore, early demonstrations of spin-photon entanglement in these cases have used strong magnetic fields to remove the degeneracy of the trions, thereby reestablishing optical Λ systems [24–27]. The proposal of Ref. [20] requires that the spin states and their optical excitations form an optical Π system and therefore the use of high magnetic field is detrimental.

Schwartz and coworkers have demonstrated a proof-of-concept realization of the Ref. [20] proposal, using the spin of the dark exciton (DE) as the entangler [28]. The short-range electron-hole exchange interaction slightly removes the degeneracy of the DE. Therefore, a coherent superposition of the DE eigenstates naturally precesses, even in the absence of an external magnetic field. Due to the limited temporal resolution of the silicon avalanche photodetectors

used by Schwartz *et al.*, the spin is reexcited every three quarters of its precession period, instead of every quarter as in the original proposal. Schwartz and coworkers have shown that the entanglement robustness of the 1D photonic string is mainly determined by the ratio between the photon radiative time and the spin-precession time and to a lesser extent also by the ratio between the latter and the confined-spin-coherence time [28].

In this study, we use a larger number of single-photon detectors, with better quantum efficiency and an order of magnitude better temporal resolution than previously available. The enhanced temporal resolution allows an increase by a factor of 3 of the photon generation rate, exciting the entangler every quarter of its precession period while at the same time obtaining much better photon correlation statistics. Moreover, the improved temporal resolution allows complete spin tomography [29] of the spin state of the entangler, in addition to the full characterization of the polarization states of the emitted photons [30].

Thus, here we use complete time-resolved spin-multiphoton correlation measurements for characterizing the quantum state and the periodically applied process map that generates the photonic cluster. For this purpose, we develop a "fitting" algorithm that is particularly efficient and applicable to our experimental measurements. We use 144 different time-resolved two- and three-photon correlation measurements to extract the overall 8×8 physical quantum state and process map that best describes our system. Then, we apply a gradient-descent method for finding the maximal log-likelihood between the physical model and the measured data. Our method differs from the standard one in defining the gradient relative to a specific non-Euclidean metric that is adapted to the geometry of the set of physical (completely positive) process maps (or quantum states). This approach is different from known algorithms such as projected gradient descent [31–33] and more suitable for our experimental data.

We demonstrate that our improved experimental system and analysis allow us to measure the slight improvement to the generated cluster state due to the reduced decoherence of the DE spin [34] during the faster optical driving. This is important since, to begin with, the expected effect of the spin dephasing on the process map is much smaller than the effect of the finite spectral width of the radiative decay [28].

II. CLUSTER-STATE GENERATION: METHOD

At the heart of our device is a semiconductor QD. The QD contains a confined electronic-spin, which serves as the entangler qubit [20,35,36]. We define the sample growth direction, which is also the shortest dimension of the QD (about 3 nm), as the quantization z axis. The QD is embedded in a planar microcavity, formed by two Bragg-reflecting mirrors [Fig. 1(a)], facilitating efficient light harvesting by an objective placed above the QD.

The DE is an electron-hole pair with parallel spins [38–40], having two total angular momentum states of ± 2 as projected onto the QD z axis. Since the DE optical activity is weak [41], it has a long life and a long coherence time [34,39]. Upon optical excitation, the DE ($|\Uparrow\uparrow\rangle$) is excited to form a biexciton (BIE) ($|\Uparrow\Uparrow\uparrow\downarrow\rangle$). The BIE is formed by a pair of electrons in their first conduction-subband level and two heavy holes with parallel spins, one in the first and one in the second valence-subband levels. Figures 1(b) and 1(c) schematically describe the DE-BIE energy-level structure and the selection rules for optical transitions between these levels, respectively [38,42,43].

Each laser pulse (in red) excites the QD-confined DE to its corresponding BIE state. The BIE decays to the DE* level within about 370 ps by radiative recombination in which a single photon is emitted (marked in pink). The DE* then decays to the ground DE state by about 70-ps spin-preserving acoustic-phonon relaxation. The energy difference between the emitted photon and the exciting laser allows us to spectrally filter the emitted single photons.

The eigenstates of the DE and BIE are given by $|\pm X_{DE}\rangle = (|+Z_{DE}\rangle \pm |-Z_{DE}\rangle)/\sqrt{2}$ and $|\pm X_{BIE}\rangle = (|+Z_{BIE}\rangle \pm |-Z_{BIE}\rangle)/\sqrt{2}$. The energy differences between these eigenstates are about $1 \mu eV$, smaller than the radiative width of the BIE optical transition ($\simeq 3 \mu eV$) and much smaller than the spectral width of our laser pulse ($\simeq 100 \mu eV$). It follows that a coherent superposition of the DE (BIE) eigenstates precesses with a period $T_{DE} = 3.1$ ns ($T_{BIE} = 5.6$ ns), an order of magnitude longer than the BIE radiative time.

The DE and BIE act as spin qubits. Angular-momentum conservation during the optical transitions between these two qubits implies the following π-system selection rules [34]:

$$|\Uparrow\uparrow\rangle \xleftrightarrow{|+Z\rangle} |\Uparrow\Uparrow\downarrow\uparrow\rangle,$$
$$|\Downarrow\downarrow\rangle \xleftrightarrow{|-Z\rangle} |\Downarrow\Downarrow\uparrow\downarrow\rangle. \tag{1}$$

where $|+Z\rangle$ ($|-Z\rangle$) is a right- (left-) hand circularly polarized photon propagating along the $+Z$ direction. It thereby follows that a laser pulse polarized as $|+X\rangle = (|+Z\rangle + |-Z\rangle)/\sqrt{2}$ coherently excites a superposition $\alpha|\Uparrow\uparrow\rangle + \beta|\Downarrow\downarrow\rangle$ of the DE spin-qubit states to a similar superposition $\alpha|\Uparrow\Uparrow\uparrow\downarrow\rangle + \beta|\Downarrow\Downarrow\uparrow\downarrow\rangle$ of the BIE states. The BIE then radiatively decays into an entangled spin-photon state $\alpha|\Uparrow\uparrow\rangle|+Z\rangle + \beta|\Downarrow\downarrow\rangle|-Z\rangle$. Therefore, the excitation and photon emission act as a two-qubit entangling controlled-NOT (CNOT) gate between the spin and the photon.

The method for generating the cluster state is described in Fig. 1(d). The confined DE is resonantly excited
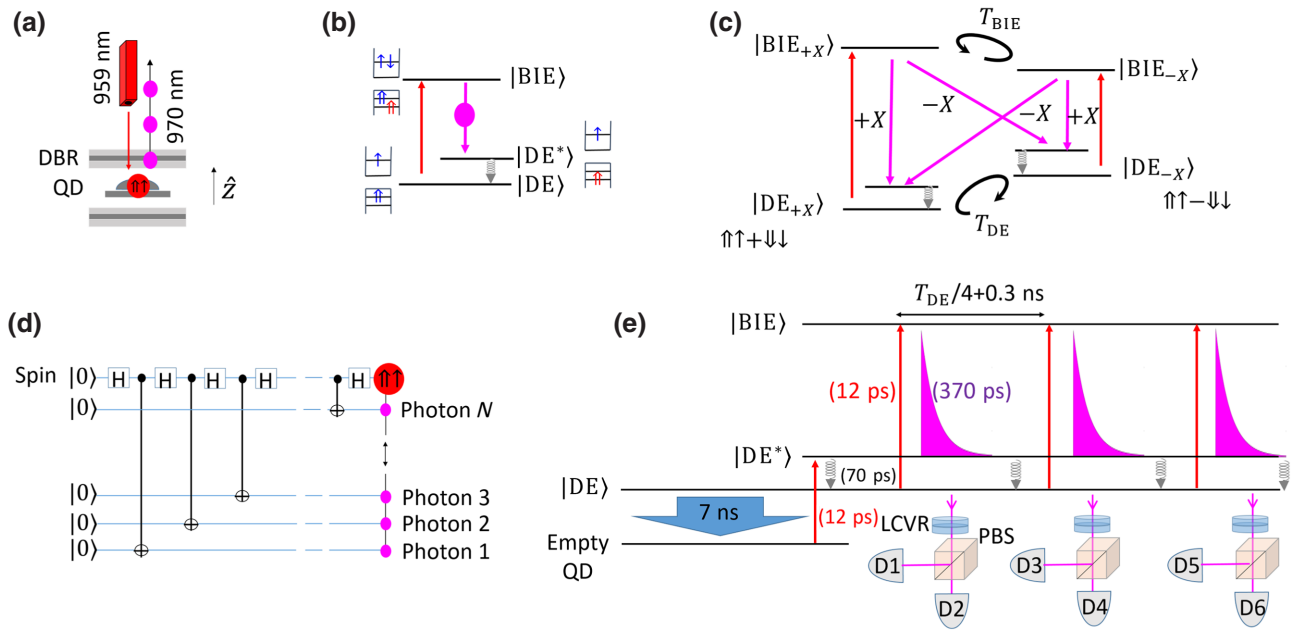
FIG. 1. (a) A schematic description of the QD-based device: DBR, distributed Bragg reflector. (b) The energy levels of the DE-DE*-BIE system and the transitions between these levels. Each laser pulse (red upward-pointing arrow) excites the DE and photogenerates a BIE. The BIE then decays to an excited DE* by emitting a single-photon (downward pink arrow). The DE* then decays to its ground level by emitting an acoustic-phonon (curly downward-pointing arrow). (c) The BIE-DE*-DE energy levels and the polarization-selection rules for the optical transitions. Here, $+X$ $(-X)$ describes a horizontally (vertically) rectilinearly polarized optical transition. The short-range electron-hole exchange interaction removes the degeneracy between the two eigenstates of both the DE and the BIE. A coherent superposition of the DE (BIE) eigenstates precesses with a period marked by T_{DE} (T_{BIE}). (d) The cluster-state repeating protocol containing Hadamard gates acting on the QD confined spin followed by a two-qubit controlled-NOT (CNOT) gate, which entangles the spin polarization with the polarization of the emitted photons. (e) The experimental setup, pulse sequence, photon emissions, and detection for realizing and characterizing the cluster state. The blue downward-pointing broad arrow is an optical-depletion 7-ns-long pulse [37], which depletes the QD of carriers. The upward-pointing arrows are 12-ps-long π-area laser pulses, while the downward-pointing pink exponential decays represent the emitted photons. We project the polarization of the photons using liquid-crystal variable retarders (LCVRs) and polarizing beam splitters (PBSs) while looking for up to three photon correlations.

repeatedly by a laser pulse to its corresponding BIE. The BIE decays radiatively by emitting a photon. The excitation and photon emission act as a two-qubit CNOT gate that entangles the emitted photon-polarization qubit and the spin qubit, thus adding a photon to the growing photonic cluster. The excitation pulses are timed such that between the pulses, the DE spin precesses by one quarter of its precession period. This temporal precession can be ideally described as a unitary Hadamard gate acting on the spin qubit only. The combination of the CNOT two-qubit gate and the Hadamard one-qubit gate forms the basic cycle of the protocol, which when repeated periodically generates the entangled spin-plus-photons cluster state [20].

For the experimental realization of the cluster protocol and the characterization of the generated state, we use the experimental setup described in Fig. 1(e). The QD is first optically emptied of carriers, making it ready for initialization. The first 7-ns-long optical pulse (blue downward-pointing arrow) depletes the QD of charges and the remaining DE [37]. Then, using a horizontally

polarized 12-ps optical π pulse, we write the DE spin state to the DE* state. This is possible due to small-mixing between the bright exciton (BE) and the DE [40]. The pulsed polarization defines the DE* initial spin state. The DE* then relaxes to its ground DE state, making the QD ready for implementing the cluster protocol. A sequence of resonantly tuned linearly polarized π-area laser pulses is then applied to the QD. Each pulse results in the emission of a photon from the BIE-DE optical transition of the QD. During the last emission, the BIE-spin evolution can be conveniently used as a resource for the DE-spin tomography [29].

To characterize the generated multiqubit quantum state, we project the polarization of the detected photons onto six different polarization states using liquid-crystal variable retarders (LCVRs) and polarizing beam splitters (PBSs). We then use highly efficient transmission gratings to spectrally filter the emitted photons from the laser light. The photons are eventually detected by six efficient ($> 80\%$) fast single-photon superconducting detectors

with a temporal resolution of about 30 ps. We use a laser sync and consecutive one-, two-, and three-photon correlations for the analysis presented above.

III. CLUSTER-STATE CHARACTERIZATION

The robustness of the cluster-state entanglement is characterized using three cycles of the repeated protocol. The characterization is done by correlating one, two, and three detected photon events. In all cases the last detected photon is used for the tomography of the DE spin. We use two different orthogonal $+X$ and $+Y$ linearly polarized excitation pulses, respectively [29]. The $+X$-polarized laser pulse promotes the DE state to a similar superposition of BIE states, while the $+Y$ excitation introduces a $\pi/2$ phase shift to the superposition [29]. In addition, we utilize the BIE-state evolution during its radiative decay back to DE* to measure the degree of circular polarization ($D_{\rm cp}$) of the emission as a function of time:

$$D_{\rm cp}(t) = \frac{P_{+Z}(t) - P_{-Z}(t)}{P_{+Z}(t) + P_{-Z}(t)}, \qquad (2)$$

where P_j represents the detected photon-polarization projection onto the j basis. By fitting the measured $D_{\rm cp}(t)$ to a central spin-evolution model that we have recently developed for QD-confined charge carriers [29], we accurately extract the DE-spin state at the time of its optical excitation.

As we implement the protocol, we perform full tomographic measurements of the growing quantum state. First, we measure the initialized DE state. Then we apply one cycle of the protocol and measure the resulting spin-plus-one-photon state. Finally, we apply a second cycle of the protocol and measure the spin-plus-two-photons state.

In Fig. 2, we present a small set of the measurements used to deduce the spin, spin-plus-one-photon, and spin-plus-two-photons quantum states and the process map of the periodic cycle of the cluster protocol. The first row shows $D_{\rm cp}$ measurements characterizing the initialized spin, the second row shows the $D_{\rm cp}$ of the correlated spin-plus-one-photon state after the photon is projected onto a $+Y$-polarization basis, and the third row shows the $D_{\rm cp}$ of the correlated spin-plus-two-photons state after both photons are projected onto a $+Y$-polarization basis. Each row differs from the row above it by the application of one additional cycle of the protocol. In all measurements shown in Fig. 2, the DE is initialized to the $-X$ state. In each row, the left panel displays the time-resolved photoluminescence (PL) and the center panel (right panel) displays the time-resolved $D_{\rm cp}$ measured after $+X$- ($+Y$-) polarized excitation of the final spin. By fitting the $D_{\rm cp}$ correlation measurements, we extract the following spin, spin-plus-one-photon, and spin-plus-two-photons
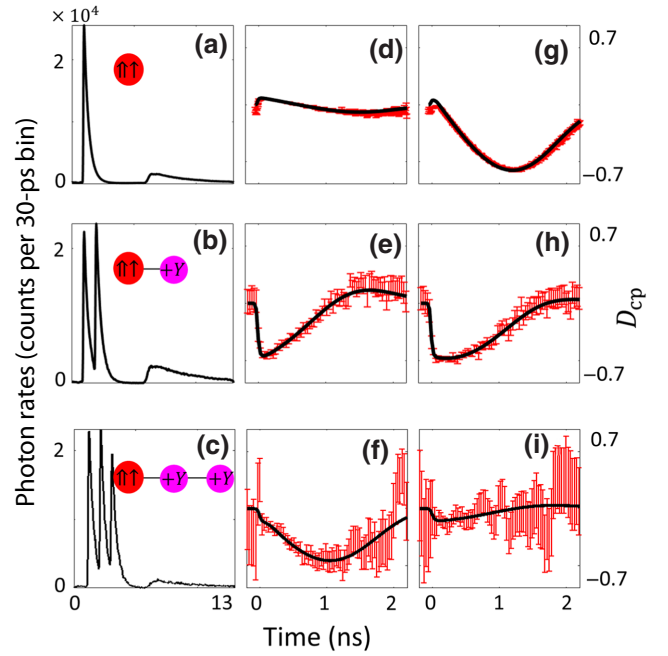

FIG. 2. Examples of one-, two-, and three-photon correlation measurements performed in characterizing the photonic cluster state. (a)–(c) Time-resolved PL measurements of the BIE-DE optical transition following one-, two-, and three-pulse excitations, respectively. (d)–(f) The time-resolved degree of the circular-polarization measurements $D_{\rm cp}(t) = \frac{P_{+Z}(t) - P_{-Z}(t)}{P_{+Z}(t) + P_{-Z}(t)}$ of the last detected photon, using a horizontally polarized ($+X$) excitation pulse. (g)–(i) The same as (g), (e), and (f), but using a diagonally linearly polarized excitation pulse ($+Y$). The red data points describe the measured data and the solid black line describes the fitted model calculations (see Ref. [29]). From the fitted model, we extract the spin, spin-plus-one-photon, and spin-plus-two-photons polarization-projection measurements.

polarization-projection measurements, respectively:

$$[S_X, S_Y, S_Z] = [-0.73, 0.05, 0.06], \qquad (3)$$

$$[P_Y^{(1)} S_X, P_Y^{(1)} S_Y, P_Y^{(1)} S_Z] = [0.01, 0.16, -0.59], \qquad (4)$$

$$[P_Y^{(1)} P_Y^{(2)} S_X, P_Y^{(1)} P_Y^{(2)} S_Y, P_Y^{(1)} P_Y^{(2)} S_Z] = [0.03, -0.49, -0.08], \qquad (5)$$

where $P_j^{(i)}$ represents the polarization projection of the ith photon in the string, onto the j polarization basis, and S_j is the DE-spin polarization, projected onto the j basis. The uncertainties in the projection measurements are about 0.01, 0.02, and 0.04 for the spin, spin-plus-one-photon, and spin-plus-two-photons polarization-projection measurements [Eqs. (3), (4), and (5)], respectively. The counting rates that we obtain are typically about 10^5 single-photon events per detector per second, 1000 two-photon, and ten three-photon correlation

events per second, reflecting a total system detection efficiency of about 1%. The numbers of polarization-projected correlation events used for the analysis presented here are typically 10^5, 7000, and 900 for consecutive one-, two-, and three-photon events, respectively.

For a perfect initialization and application of the process, we expect the deduced polarization-projection measurements [Eqs. (3), (4), and (5)] to be [-1,0,0], [0,0,-1], and [0,-1,0], respectively. Here, however, the DE spin is initialized to the $-X$ state with a polarization degree of only 0.73, due to the limited efficiency of the depleting pulse [37]. Moreover, each additional cycle of the protocol reduces the expected maximal D_{cp} by approximately 20%, as expected for the finite localizable entanglement of the process map [28,44].

The measured correlations are used to infer directly the spin-plus-one-photon two-qubit state, obtained by applying one cycle of the protocol, the spin-plus-two-photons state, obtained by applying two cycles of the protocol, and a full process tomography of the periodic cycle of the cluster protocol.

To measure the spin-plus-one-photon density matrix [displayed in Fig. 3(a)], we use a set of 12 DE-photon $D_{cp}(t)$ correlation measurements. Two of those measurements are displayed in Figs. 2(e) and 2(h). The measured density matrix has a fidelity of $F = 0.77 \pm 0.04$ with the maximally entangled Bell state. To measure the spin-plus-two-photons three-qubit density matrix [displayed in

Fig. 3(b)], we use a set of 72 $D_{cp}(t)$ DE-plus-two-photons correlation measurements. Two of those measurements are displayed in Figs. 2(f) and 2(i). The measured spin-plus-two-photons density matrix has a fidelity of 0.68 ± 0.07 with the maximally entangled three-qubit state.

We produce the cluster state by repeatedly applying the same process, as shown in the protocol of Fig. 1(d). As a result, one can fully characterize the cluster state for any number of qubits if the single-cycle process map is known [28]. Ideally, the process map contains a CNOT and a Hadamard gate. It maps the 2×2 spin-qubit density matrix into a 4×4 density matrix representing the entangled spin-photon state. The process map Φ can be fully described by a 4×16 positive and trace-preserving map with 64 real matrix elements.

We use the convention $\Phi(\hat{\rho}_{DE}) = \sum\limits_{\alpha,\beta,\gamma} \Phi^\gamma_{\alpha\beta} \rho^{DE}_\gamma \hat{\sigma}_\alpha \hat{\sigma}_\beta$, where $\hat{\rho}_{DE} = \sum\limits_\gamma \rho^{DE}_\gamma \hat{\sigma}_\gamma$ is the density matrix that describes the input DE state and $\Phi(\hat{\rho}_{DE})$ describes the DE-plus-one-photon state after one application of the process to the input DE state. The sums are taken over $\alpha, \beta, \gamma = O, X, Y, Z$, where $\hat{\sigma}_0$ is the identity matrix and $\hat{\sigma}_X, \hat{\sigma}_Y, \hat{\sigma}_Z$ are the corresponding Pauli matrices. The 64 real parameters $\Phi^\gamma_{\alpha\beta}$ thus fully specify Φ.

Figure 3(c) shows the results of the full tomographic measurements of the process map. For acquiring these measurements, we initialize the DE spin state to six different states from three orthogonal bases [40]. For each
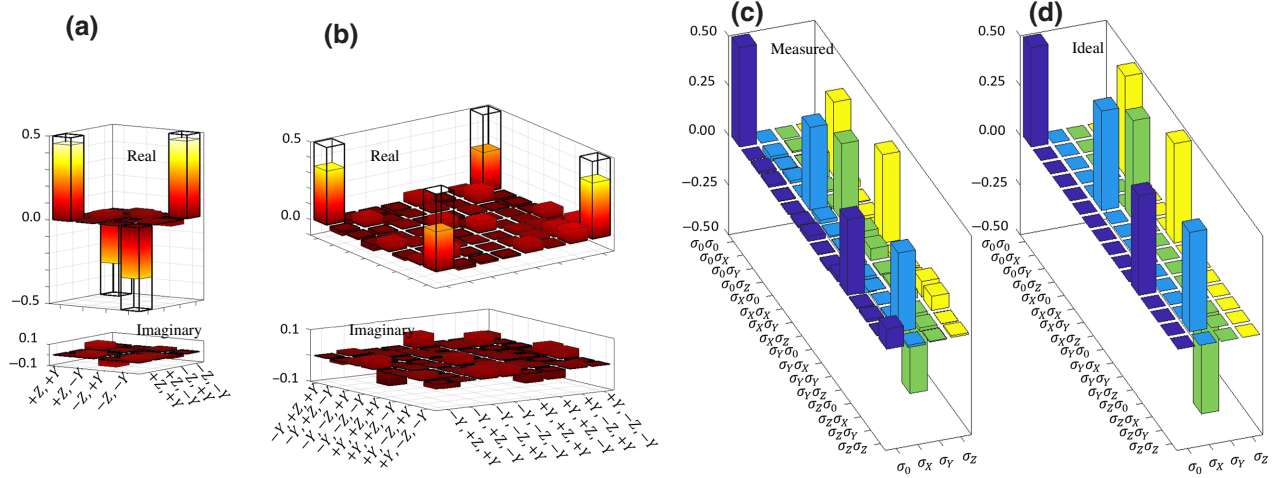

FIG. 3. (a) The measured DE-plus-one-photon density matrix. (b) The measured DE-plus-two-photons density matrix. In (a) and (b), the colored bars represent measured density-matrix elements, while the empty bars represent the ideal maximally entangled two- and three-qubit states. The fidelity of the measured density matrix to the ideal one is $F = 0.77 \pm 0.04$ in (a) and $F = 0.68 \pm 0.07$ in (b). In both cases, the DE spin is initialized to the $|-X_{DE}\rangle$ state with a measured fidelity of $F = 0.86 \pm 0.02$ and then one or two applications of the process. The process map Φ, which describes the evolution of the system in each cycle of the protocol, is given by $\Phi(\hat{\rho}_{DE}) = \sum\limits_{\alpha,\beta,\gamma} \Phi^\gamma_{\alpha\beta} \rho^{DE}_\gamma \hat{\sigma}_\alpha \hat{\sigma}_\beta$, where $\hat{\rho}_{DE} = \sum\limits_\gamma \rho^{DE}_\gamma \hat{\sigma}_\gamma$ is the density matrix that describes the input DE state and $\Phi(\hat{\rho}_{DE})$ describes the DE-plus-one-photon state after applying the process on the input DE qubit. Here, α, β, and γ run over O, X, Y, and Z, where $\hat{\sigma}_0$ is the identity matrix and $\hat{\sigma}_X$, $\hat{\sigma}_Y$, and $\hat{\sigma}_Z$ are the corresponding Pauli matrices. The 64 real parameters $\Phi^\gamma_{\alpha\beta}$ thus fully specify Φ. (c) The process map $\Phi^\gamma_{\alpha\beta}$ as measured by the quantum process tomography. The matrix elements of $\Phi^\gamma_{\alpha\beta}$ are presented such that the rows correspond to the indices $\alpha\beta$ of the DE-plus-one-photon output state and the columns correspond to the index γ of the input DE state. (d) The process map $\Phi^\gamma_{\alpha\beta}$, calculated assuming the ideal protocol (CNOT and Hadamard gates), as in Fig. 1(d).

of those six states, we use two $D_{cp}(t)$ single-photon measurements like the measurements displayed in Figs. 2(d) and 2(g) for tomography. We then apply one cycle of the protocol for each initialization and measure the resulting spin-plus-one-photon states by projecting the first photon onto different orthogonal polarization bases [30] and correlating it with the $D_{cp}(t)$ of the second photon. For characterizing each of those six spin-plus-one-photon states, we use 12 $D_{cp}(t)$ two-photon correlations measurements like the ones presented in Figs. 2(e) and 2(h).

To obtain the physical process map that best fits our measured results, we use a specifically developed edge-sensitive twisted-gradient-descent minimization method (see Appendix B). It is well known that the space of physical completely positive (CP) maps can be identified with a conelike space where any unitary process sits on an extremal ray of the cone. To find the best CP fit of Φ therefore requires minimization of a known function F (representing minus log likelihood) over this cone. Gradient descent tries to find the minimum of a function $F(x)$ by going roughly along the gradient lines of F. Our developed approach uses an edge-sensitive twisted-gradient descent in order to prevent our gradient-descent solution from getting stuck in the boundary of the physically allowed conelike region.

Figures 3(c) and 3(d) present the physical CP-process map obtained using this method. We compare the acquired physical process with the ideal unitary process of the cluster protocol. The fidelity [28,45] between the measured and ideal process is 0.825 ± 0.01. We note that the obtained fidelity is marginally better than in the previous demonstration, 0.81 ± 0.1 [28]. The slightly better fidelity reflects the fact that during the threefold shorter time between the optical excitations, the DE maintains its spin coherence better. The uncertainty in the measured fidelity is evaluated by propagating the statistical uncertainties in the single-photon counts (typically 10^5 counts) and the two-photon correlation counts (typically 7000 events). We note that the obtained uncertainty here is an order of magnitude better than that in Ref. [28]. The improved accuracy reflects the facts that (a) we use here more statistics and (b) that in Ref. [28], some density-matrix elements are deduced from experiments in which two cycles of the protocol are applied. The latter leads to quadratic dependence on the physical process, in contrast to the linear dependence when only one cycle of the process is applied, as is the case here.

IV. DISCUSSION

We characterize the robustness of the entanglement in the 1D cluster state using the notion of localizable entanglement (LE) [47]. The LE is the negativity [46] between two qubits in the cluster after all the other qubits are projected onto a suitable polarization basis. The LE decays

exponentially with the distance between the qubits [28,44]:

$$N(d) = N_{nn} \exp\left(-(d-1)/\zeta_{LE}\right), \qquad (6)$$

where N_{nn} is the negativity between nearest-neighbor qubits, d is the distance between the qubits, and ζ_{LE} is the characteristic decay length of the LE. In Fig. 4, we plot using pink circles the LE in the state of a spin plus N photons, obtained from the measured process map, as a function of the distance between two qubits in the string. As expected, the LE in the 1D cluster state decays exponentially with the distance between the two qubits [44]. Figure 4 shows that the entanglement in the cluster persists up to six photons. This presents an improvement over Ref. [28], resulting from the reduction in the DE spin decoherence between the optical pulses.

The negativity between two nearest-neighbor and next-nearest-neighbor qubits can be directly obtained from our quantum state tomography. The entanglement between the DE and the photon emitted after one cycle of the protocol is obtained from the density matrix of the DE plus one photon in Fig. 3(a), which has a negativity of $N = 0.27 \pm 0.03$. This negativity is marked as a purple data point in Fig. 4. Similarly, the spin-plus-two-photons three-qubit state resulting from application of two cycles of the protocol is represented by the three-qubit density matrix, displayed in Fig. 3(b). The negativity of the density matrix of the two external qubits, after projecting the central qubit
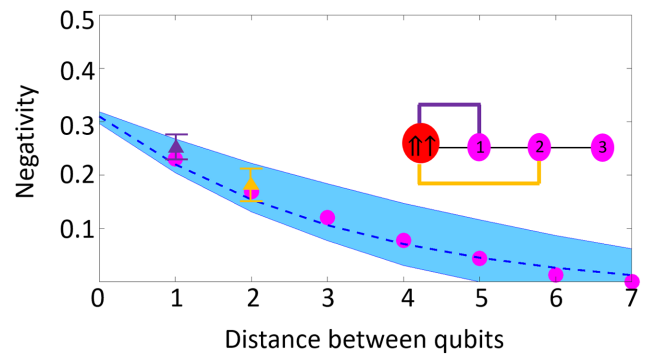

FIG. 4. The localizable entanglement (LE, pink circles) in the generated state versus the distance between two qubits in the string. The pink circles correspond to the LE between qubits m and $m + d$ in the state of DE plus N photons obtained using the measured process map. The dashed lines represent the best fit to an exponential decay law $N(d) = N_{nn} \exp\left(-(d-1)/\zeta_{LE}\right)$, where N_{nn} is the negativity [46] between nearest-neighbor qubits, d is the distance between the qubits, and ζ_{LE} is the characteristic decay length of the LE. The light-blue shaded area represents one standard deviation of the uncertainty in the measurements determining the process map. The purple and yellow data points represent the directly measured LE of the DE and the first emitted photon in a two- and a three-qubit string, respectively, acquired from the complete tomographic measurements of those states presented in Figs. 3(c) and 3(d).

onto the X polarization basis, is $N = 0.18 \pm 0.05$, marked by the yellow point in Fig. 4.

We note here that the generation of the cluster state is deterministic, namely, every laser pulse results in an entangled photon emission, at a rate of over 1 GHz. Since the light-harvesting efficiency of our system is currently only about 1%, we detect sequentially three and four photons at rates of a few hundred and just a few Hz, respectively. Feasible improvement of the collection efficiency to about 50%, for example [48–50], will result in the possible detection of 20 sequentially emitted photons at a rate of a few hundred Hz. In addition, by using the heavy hole instead of the DE as an entangler, while optimizing its precession rate by an externally applied magnetic field we have recently succeeded in generating indistinguishable photons in a cluster state while increasing the localizable entanglement exponential characteristic decay length to ten photons [51].

In summary, we demonstrate a gigahertz-rate deterministic generation of entangled photons in a cluster state, which is 3 times faster than previously demonstrated. We develop a method for spin-multiphoton quantum state tomography and for characterizing the periodic process map that generates the photonic cluster state. Using this method, we show that the enhanced cluster generation rate also improves the robustness of the entanglement in the generated multiphoton state. The measured process map has a fidelity of 0.83 to the ideal one and the entanglement in the cluster state persists up to six consecutive qubits. Our studies combined with further feasible optimizations of the device may lead to implementations of quantum communication and efficient distribution of quantum entanglement between remote nodes.

APPENDIX A: THE PROCESS LIKELIHOOD FUNCTION

The basic (single-cycle) process taking the QD spin into a spin plus an emitted photon is described by a process map Φ taking a one-qubit state into a two-qubit state. Expanding these quantum states in terms of Pauli matrices allows us to write the map as

$$\rho = \sum r_\mu \sigma^\mu \mapsto \Phi(\rho) = \sum r_\mu \phi^\mu_{\nu\lambda} \sigma^\nu \otimes \sigma^\lambda.$$

Here, $\phi^\mu_{\nu\lambda}$ with $\mu\nu\lambda \in \{0, x, y, z\}$ are 64 real coefficients that define the process map Φ.

The trace-preserving condition $Tr\Phi(\rho) = Tr\rho \forall\rho$ fixes 4 out of the 64 coefficients $\phi^\mu_{\nu\lambda}$, namely, it requires that $\phi^\mu_{00} = 1/2\delta_{\mu 0}$. We wish to estimate the other 60 parameters by finding the best fit to the experimental data.

In an experiment where the initial spin is $\vec{s}$ and the emitted photon is projected onto the state of spin [52] $\vec{p}$, we would ideally expect the measured rate R of the photon emission and the final spin $\vec{S}$ to satisfy $\phi_{\nu\lambda\mu} s_\mu p_\lambda = R S_\nu$. Here, s, p, and S are four vectors, the zeroth component of which equals 1, and their spatial components are $\vec{s}$, $\vec{p}$, and $\vec{S}$. Repeating such measurements for six different spin polarizations $\vec{s}$ and six different photon polarizations $\vec{p}$ gives $6 \times 6 \times 4 = 144$ equations for the 60 unknown components of Φ.

A straightforward approach to determining Φ is then to use a least-squares method, minimizing the expression $F_0 = \sum_{p,s,\nu} \frac{1}{\Delta^2_{ps\nu}} \left[\phi_{\nu\lambda\mu} s_\mu p_\lambda - R S_\nu \right]^2$. Here, F_0 is essentially a Gaussian (or χ^2) approximation of the log-likelihood and $\Delta_{ps\nu}$ are the error estimates of the corresponding measurement. A slightly more sophisticated approach would recall that the appearance of each of the six initial polarizations $\vec{s}$ in 24 different sums can potentially make the errors correlated. One way to take this into consideration is to use a more complicated square sum constructed using a nondiagonal covariance matrix. A completely equivalent method consists of defining new variables $\vec{s}'$ representing the actually measured initial polarization of the DE [29] and using the new sum of the square-error function $\tilde{F}_0 = \tilde{F}_0(\phi, s')$ defined by [53]

$$\tilde{F}_0(\phi, s') = \sum_{p,s,\nu} \frac{1}{\Delta^2_{ps\nu}} \left[\phi_{\nu\lambda\mu} s'_\mu p_\lambda - R S_\nu \right]^2$$
$$+ \sum_s \sum_{i=1}^3 \left(\frac{s'_i - s_i}{\Delta s_i} \right)^2.$$

Minimization of this expression with respect to s' yields a standard square sum $F_0(\phi)$ corresponding to the correct nondiagonal covariance matrix. We look for a minimum of $\tilde{F}_0(\phi, s')$ with respect to both the process map ϕ and the initialization polarizations s'.

APPENDIX B: COMPLETELY POSITIVE CONDITION AND TWISTED-GRADIENT DESCENT

It is well known that to be physically acceptable, a process map Φ must be CP. A process map is CP if and only if the associated Choi matrix, which may be defined (up to unimportant normalization factor) by

$$C_\Phi = \sum \phi^\mu_{\nu\lambda} \overline{\sigma_\mu} \otimes \sigma^\nu \otimes \sigma^\lambda, \qquad \text{(B1)}$$

is positive (semidefinite), $C_\Phi \geq 0$. The bar over σ_μ denotes complex conjugation and we make no distinction here between lower and upper indices. In general, the Choi matrix C_Φ is a (complex) Hermitian 8×8 matrix that may be used as an alternative description of Φ.

Simple-minded naive minimization of F_0 leads to a process map that is not CP and hence not physically acceptable. To understand why this happens, recall that our process is very close to an idealized process that is unitary. Any unitary process is an extreme point of the cone of CP maps and has a rank-1 Choi matrix. In other words, for a unitary process, seven out of the eight eigenvalues of the Choi matrix vanish. Our Φ, being close to unitary, therefore has seven very small Choi matrix eigenvalues. It is thus not surprising that very small experimental errors can lead us to estimate some of these eigenvalues as negative, in contradiction with the CP condition. (Had our Φ been equal to the ideal unitary map, a small random error in each eigenvalue would lead to a non-CP map with probability $127/128 = 0.992$.) In other words, the encountered difficulty is actually a good sign, indicating that our process has quite low decoherence.

The finding of the best CP fit of Φ therefore requires minimization of a known function F (representing minus log likelihood) over the subset of CP maps [54,55], which, as explained above, may be identified (through the Choi representation) with the cone of positive matrices. This is closely related to the extensively studied field of convex optimization. We choose, however, to devise a method of our own (explained below), which is a variant of the well-known gradient descent and perfectly fits our needs.

Gradient descent tries to find the minimum of a function $F(x)$ by going roughly along gradient lines of F. It corresponds to a (numerically discretized) solution to the equation $d/dtx^i = -g^{ij}\partial_j F(x)$. The (inverse) metric tensor g^{ij} is often taken to be the standard Euclidean metric δ_{ij}. Such a choice is not mandatory and, in fact, one may choose any (positive) metric. We suggest using a smarter choice of the metric in order to prevent our gradient-descent solution from getting stuck in the boundary of the physically allowed region.

It is easiest to understand our approach by considering minimization over a simple region such as $\{(x,y) \in \mathbb{R}^2 \mid x,y \geq 0\}$. In this case, our approach to the minimization of $F(x,y)$ would correspond to using iteration steps with $(\Delta x, \Delta y) \propto (x\partial_x F, y\partial_y F)$. Assuming that both derivatives of F are $O(1)$, one sees that if our approximate estimate (x,y) of the minimizer is very close to one of the boundaries, e.g., if it has $x \ll 1$ and $y = O(1)$, then the next step $(\Delta x, \Delta y)$ would adapt to this fact by being almost parallel to the y axis. One can then go a long, approximately $O(1)$, distance along this direction without crossing boundary. This is in contrast to hitting the boundary after a distance $O(x) \ll 1$, as would result from using the standard metric $g_{ij} = \delta_{ij}$.

Since the CP condition is easier to formulate in terms of Choi matrices, let us consider the (square sum) function that we want to minimize as a function $F(A)$ over the (real vector space) of Hermitian matrices [56]. The standard Euclidean gradient of F may be identified with the matrix ∇F, the elements of which are $(\nabla F)_{ij} = \partial F/\partial a_{ji}$. (This relation may be a bit confusing, since the elements a_{ij} of A are complex.) An equivalent and possibly more rigorous definition starts by expressing A as $A = \sum a_\alpha \Xi_\alpha$, where $a_\alpha \in \mathbb{R}$ and $\{\Xi_\alpha\}$ are some basis for the space of Hermitian matrices, which is orthonormal in the sense $Tr(\Xi_\alpha \Xi_\beta) = N\delta_{\alpha\beta}$ with some normalization N. Note that our A, being a process Choi matrix, is already given to us in such a form by Eq. (B1). One can then write $\nabla F = \sum \Xi_\alpha \partial_\alpha F$.

The gradient that we use corresponds to a nonflat Riemanian metric and may be expressed as $\tilde{\nabla} F = \sqrt{A}(\nabla F)\sqrt{A}$ (where ∇F is as above). We therefore look for a minimum of F over the set of positive (semidefinite) matrices by using a gradient-descent step of the form

$$A \mapsto A + \Delta A, \quad \Delta A = -q\sqrt{A}(\nabla F)\sqrt{A}.$$

Here, $q > 0$ is a scalar chosen so that $F(A + \Delta A)$ is minimal under the constraint $A + \Delta A \geq 0$. Note that if $\nabla F = O(1)$, then the positivity constraint allows q to remain $O(1)$ even if A is very close to the boundary of the cone of positive matrices. All our process-map estimations are obtained using this minimization scheme, which we implement using MATHEMATICA^{TM}.

Although the basic method described above works reasonably well, we find that some extra improvement [57] is gained if after each step we push A slightly away from the boundary of the allowed region by updating it as $A \to (1 - \varepsilon)A + 1/2\varepsilon I$ with $\varepsilon \ll 1$. (We suspect that the need for this step might be related to the finite precision of the numerical calculations.) We increase or decrease ε dynamically during the computation, depending on the performance of the previous iteration step. In practice, ε ranges between 10^{-4} and 10^{-10} and scales roughly as 2–3 times the minimal eigenvalue of A.

The modified gradient-descent method described here is quite general and can be applied to any $F(A)$. In practice, our $F(A)$ is of the form $F(A) = F_0(A) + \sum_{\mu=0}^{3} \lambda_\mu Tr(A(\sigma_\mu \otimes I \otimes I))$, where $F_0(A)$ is the square sum described in Appendix A and the second term consists of four Lagrange multipliers required to enforce the normalization condition [58] $\phi_{00}^\mu = 1/2\delta_{\mu 0}$. The values of the multipliers λ_μ at each iteration step are easily determined numerically by requiring that $\Delta A = -q\sqrt{A}(\nabla F)\sqrt{A}$ does not break the normalization condition. This amounts to demanding the partial trace $Tr_{2,3}(\sqrt{A}(\nabla F)\sqrt{A})$ to vanish, which is just a linear set of equations for λ_μ.

APPENDIX C: COMPARISON BETWEEN TWISTED AND PROJECTED-GRADIENT-DESCENT METHODS

We compare our process-map reconstruction method to an existing method [31,32]. We run our twisted-gradient-descent algorithm and a projected gradient algorithm on the same data, corresponding to a simulation of random processes.

We choose (many) random unitary maps and add a small amount of noise to obtain a (nonunitary) process map Φ with low impurity (about 5%). Then, we simulate the results of the experiment corresponding to this and calculate an estimation for the process map (from the simulation data) using four different cases:

(1) We use our twisted-gradient descent to look for the minimum of $\chi^2 \sim \sum (p_i - f_i)^2/f_i$. Here, f_i is a measured frequency of a certain simulation, while p_i is calculated from the fitting method.

(2) We use our twisted-gradient descent to look for a maximum of the log-likelihood function $L \sim -\sum (f_i Log(p_i/f_i))$. (According to the central-limit theorem, $L \sim \chi^2$. However, the equality is not exact for finite data.)

(3) We use the projected gradient descent to minimize χ^2.

(4) We use the projected gradient descent to maximize the log-likelihood.

In these simulations, we ignore state-preparation-and-measurement (SPAM) errors that exist in the actual experiment. We typically use 1000 counts per measurement and

process purities of about 95%. We note that ensembles of different purities may lead to different results.

Figure 5 presents a comparison between the four cases. For each case, we calculate the cost function after each iteration and since we know the true Φ, we also calculate the infidelity ($1 - F$, where F is the fidelity) between Φ and its estimates, indicating the success of the method. It seems that the cost function of our twisted-gradient-descent method converges a little faster than the projected gradient method, both for the χ^2 and the log-likelihood cost functions. The infidelity converges to the same value (within the uncertainties) in all cases, as one expects. However, the convergence is faster in the twisted gradient than in the projected method. It also appears that the difference in the convergence speed is more pronounced for the log-likelihood than for the χ^2.

To summarize the comparison, it looks as though the twisted-gradient method has a small edge over the projected method, with the log-likelihood cost function having a small advantage over χ^2.
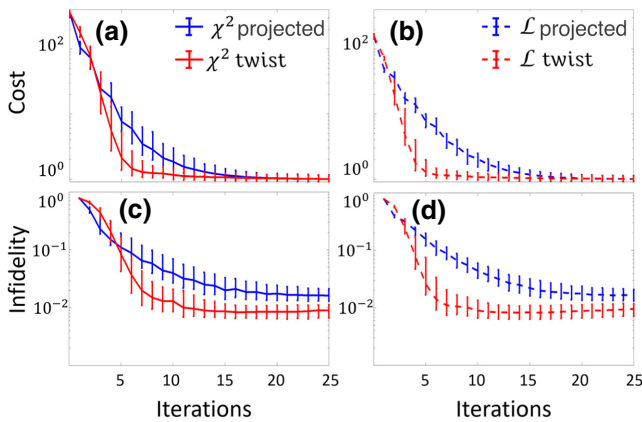

FIG. 5. A comparison between the twisted (red lines) and projected (blue lines) gradient-descent methods using χ^2 (solid lines) and the log-likelihood (dashed lines) cost function: (a),(b) the cost function; (c),(d) the infidelity ($1 - F$, where F is the fidelity) between the calculated and known processes. We average the cost and the infidelities over many random processes with inflicted impurities of about 5%. The nth number in (a)–(d) is the value attained after n iteration steps.

[1] R. Raussendorf and H. J. Briegel, A One-Way Quantum Computer, Phys. Rev. Lett. **86,** 5188 (2001).

[2] R. Raussendorf, D. E. Browne, and H. J. Briegel, Measurement-based quantum computation on cluster states, Phys. Rev. A **68,** 022312 (2003).

[3] H. J. Briegel, D. E. Browne, W. Dür, R. Raussendorf, and M. Van den Nest, Measurement-based quantum computation, Nat. Phys. **5,** 19 (2009).

[4] H.-J. Briegel, W. Dür, J. I. Cirac, and P. Zoller, Quantum Repeaters: The Role of Imperfect Local Operations in Quantum Communication, Phys. Rev. Lett. **81,** 5932 (1998).

[5] M. Zwerger, W. Dür, and H. J. Briegel, Measurement-based quantum repeaters, Phys. Rev. A **85,** 062326 (2012).

[6] M. Zwerger, H. J. Briegel, and W. Dür, Universal and Optimal Error Thresholds for Measurement-Based Entanglement Purification, Phys. Rev. Lett. **110,** 260503 (2013).

[7] K. Azuma, K. Tamaki, and H.-K. Lo, All-photonic quantum repeaters, Nat. Commun. **6,** 6787 (2015).

[8] H. J. Briegel and R. Raussendorf, Persistent Entanglement in Arrays of Interacting Particles, Phys. Rev. Lett. **86,** 910 (2001).

[9] M. Hein, J. Eisert, and H. J. Briegel, Multiparty entanglement in graph states, Phys. Rev. A **69,** 062311 (2004).

[10] P. Walther, K. J. Resch, T. Rudolph, E. Schenck, H. Weinfurter, V. Vedral, M. Aspelmeyer, and A. Zeilinger, Experimental one-way quantum computing, Nature **434,** 169 (2005).

[11] N. Kiesel, C. Schmid, U. Weber, G. Tóth, O. Gühne, R. Ursin, and H. Weinfurter, Experimental Analysis of a Four-Qubit Photon Cluster State, Phys. Rev. Lett. **95,** 210502 (2005).

[12] R. Prevedel, P. Walther, F. Tiefenbacher, P. Böhi, R. Kaltenbaek, T. Jennewein, and A. Zeilinger, High-speed linear optics quantum computing using active feed-forward, Nature **445,** 65 (2007).

[13] C.-Y. Lu, X.-Q. Zhou, O. Gühne, W.-B. Gao, J. Zhang, Z.-S. Yuan, A. Goebel, T. Yang, and J.-W. Pan, Experimental entanglement of six photons in graph states, Nat. Phys. **3,** 91 (2007).

[14] Y. Tokunaga, S. Kuwashiro, T. Yamamoto, M. Koashi, and N. Imoto, Generation of High-Fidelity Four-Photon Cluster State and Quantum-Domain Demonstration of One-Way Quantum Computing, Phys. Rev. Lett. **100,** 210501 (2008).

[15] H. J. Kimble, The quantum Internet, Nature **453,** 1023 (2008).

[16] W. J. Munro, A. M. Stephens, S. J. Devitt, K. A. Harrison, and Kae Nemoto, Quantum communication without the necessity of quantum memories, Nat. Photonics **6,** 777 (2012).

[17] M. V. Larsen, X. Guo, C. R. Breum, J. S. Neergaard-Nielsen, and U. L. Andersen, Deterministic generation of a two-dimensional cluster state, Science **366,** 369 (2019).

[18] W. Asavanant, Y. Shiozawa, S. Yokoyama, B. Charoensombutamon, H. Emura, R. N. Alexander, S. Takeda, J. ichi Yoshikawa, N. C. Menicucci, H. Yonezawa, and A. Furusawa, Generation of time-domain-multiplexed two-dimensional cluster state, Science **366,** 373 (2019).

[19] J.-C. Besse, K. Reuer, M. C. Collodo, A. Wulff, L. Wernli, A. Copetudo, D. Malz, P. Magnard, A. Akin, M. Gabureac, G. J. Norris, J. I. Cirac, A. Wallraff, and C. Eichler, Realizing a deterministic source of multipartite-entangled photonic qubits, Nat. Commun. **11,** 4877 (2020).

[20] N. H. Lindner and T. Rudolph, Proposal for Pulsed On-Demand Sources of Photonic Cluster State Strings, Phys. Rev. Lett. **103,** 113602 (2009).

[21] N. Akopian, N. H. Lindner, E. Poem, Y. Berlatzky, J. Avron, D. Gershoni, B. D. Gerardot, and P. M. Petroff, Entangled Photon Pairs from Semiconductor Quantum Dots, Phys. Rev. Lett. **96,** 130501 (2006).

[22] R. Winik, D. Cogan, Y. Don, I. Schwartz, L. Gantz, E. R. Schmidgall, N. Livneh, R. Rapaport, E. Buks, and D. Gershoni, On-demand source of maximally entangled photon pairs using the biexciton-exciton radiative cascade, Phys. Rev. B **95,** 235435 (2017).

[23] Y. Kodriano, I. Schwartz, E. Poem, Y. Benny, R. Presman, T. A. Truong, P. M. Petroff, and D. Gershoni, Complete control of a matter qubit using a single picosecond laser pulse, Phys. Rev. B **85,** 241304(R) (2012).

[24] K. De Greve, L. Yu, P. L. McMahon, J. S. Pelc, C. M. Natarajan, N. Y. Kim, E. Abe, S. Maier, C. Schneider, M. Kamp, S. Höfling, R. H. Hadfield, A. Forchel, M. M. Fejer, and Y. Yamamoto, Quantum-dot spin–photon entanglement via frequency downconversion to telecom wavelength, Nature **491,** 421 (2012).

[25] W. B. Gao, P. Fallahi, E. Togan, J. Miguel-Sanchez, and A. Imamoglu, Observation of entanglement between a quantum dot spin and a single photon, Nature **491,** 426 (2012).

[26] J. R. Schaibley, A. P. Burgers, G. A. McCracken, L.-M. Duan, P. R. Berman, D. G. Steel, A. S. Bracker, D. Gammon, and L. J. Sham, Demonstration of Quantum Entanglement between a Single Electron Spin Confined to an InAs Quantum Dot and a Photon, Phys. Rev. Lett. **110,** 167401 (2013).

[27] A. Delteil, Z. Sun, W.-b. Gao, E. Togan, S. Faelt, and A. Imamoğlu, Generation of heralded entanglement between distant hole spins, Nat. Phys. **12,** 218 (2015).

[28] I. Schwartz, D. Cogan, E. R. Schmidgall, Y. Don, L. Gantz, O. Kenneth, N. H. Lindner, and D. Gershoni, Deterministic generation of a cluster state of entangled photons, Science **354,** 434 (2016).

[29] D. Cogan, G. Peniakov, Z.-E. Su, and D. Gershoni, Complete state tomography of a quantum dot spin qubit, Phys. Rev. B **101,** 035424 (2020).

[30] D. F. V. James, P. G. Kwiat, W. J. Munro, and A. G. White, Measurement of qubits, Phys. Rev. A **64,** 052312 (2001).

[31] D. S. Gonçalves, M. A. Gomes-Ruggiero, and C. Lavor, A projected gradient method for optimization over density matrices, Optim. Methods Softw. **31,** 328 (2015).

[32] E. Bolduc, G. C. Knee, E. M. Gauger, and J. Leach, Projected gradient descent algorithms for quantum state tomography, npj Quantum Inf. **3,** 44 (2017).

[33] E. S. Tiunov, V. V. Tiunova (Vyborova), A. E. Ulanov, A. I. Lvovsky, and A. K. Fedorov, Experimental quantum homodyne tomography via machine learning, Optica **7,** 448 (2020).

[34] D. Cogan, O. Kenneth, N. H. Lindner, G. Peniakov, C. Hopfmann, D. Dalacu, P. J. Poole, P. Hawrylak, and D. Gershoni, Depolarization of Electronic Spin Qubits Confined in Semiconductor Quantum Dots, Phys. Rev. X **8,** 041050 (2018).

[35] D. Loss and D. P. DiVincenzo, Quantum computation with quantum dots, Phys. Rev. A **57,** 120 (1998).

[36] D. P. DiVincenzo, The physical implementation of quantum computation, Fortschritte der Physik **48,** 771 (2000).

[37] E. R. Schmidgall, I. Schwartz, D. Cogan, L. Gantz, T. Heindel, S. Reitzenstein, and D. Gershoni, All-optical depletion of dark excitons from a semiconductor quantum dot, Appl. Phys. Lett. **106,** 193101 (2015).

[38] E. Poem, Y. Kodriano, C. Tradonsky, N. H. Lindner, B. D. Gerardot, P. M. Petroff, and D. Gershoni, Accessing the dark exciton with light, Nat. Phys. **6,** 993 (2010).

[39] I. Schwartz, E. R. Schmidgall, L. Gantz, D. Cogan, E. Bordo, Y. Don, M. Zielinski, and D. Gershoni, Deterministic Writing and Control of the Dark Exciton Spin Using Single Short Optical Pulses, Phys. Rev. X **5,** 011009 (2015).

[40] I. Schwartz, D. Cogan, E. R. Schmidgall, L. Gantz, Y. Don, M. Zieliński, and D. Gershoni, Deterministic coherent writing of a long-lived semiconductor spin qubit using one ultrafast optical pulse, Phys. Rev. B **92,** 201201(R) (2015).

[41] M. Zieliński, Y. Don, and D. Gershoni, Atomistic theory of dark excitons in self-assembled quantum dots of reduced symmetry, Phys. Rev. B **91,** 085403 (2015).

[42] M. Bayer, G. Ortner, O. Stern, A. Kuther, A. A. Gorbunov, A. Forchel, P. Hawrylak, S. Fafard, K. Hinzer, T. L. Reinecke, S. N. Walck, J. P. Reithmaier, F. Klopf, and F. Schäfer, Fine structure of neutral and charged excitons in self-assembled InGaAs/AlGaAs quantum dots, Phys. Rev. B **65,** 195315 (2002).

[43] E. L. Ivchenko, *Optical Spectroscopy of Semiconductor Nanostructures* (Alpha Science, Harrow, U.K., 2005).

[44] M. Popp, F. Verstraete, M. A. Martín-Delgado, and J. I. Cirac, Localizable entanglement, Phys. Rev. A **71,** 042306 (2005).

[45] R. Jozsa, Fidelity for mixed quantum states, J. Mod. Opt. **41,** 2315 (1994).

[46] A. Peres, Separability Criterion for Density Matrices, Phys. Rev. Lett. **77,** 1413 (1996).

[47] F. Verstraete, M. Popp, and J. I. Cirac, Entanglement versus Correlations in Spin Systems, Phys. Rev. Lett. **92,** 027901 (2004).

[48] P. Senellart, G. Solomon, and A. White, High-performance semiconductor quantum-dot single-photon sources, Nat. Nanotechnol. **12,** 1026 (2017).

[49] N. Tomm, A. Javadi, N. O. Antoniadis, D. Najer, M. C. Löbl, A. R. Korsch, R. Schott, S. R. Valentin, A. D. Wieck, A. Ludwig, and R. J. Warburton, A bright and fast source of coherent single photons, Nat. Nanotechnol. **16,** 399 (2021).

[50] K. Tiurev, M. H. Appel, P. L. Mirambell, M. B. Lauritzen, A. Tiranov, P. Lodahl, and A. S. Sørensen, High-fidelity multiphoton-entangled cluster state with solid-state quantum emitters in photonic nanostructures, Phys. Rev. A **105,** L030601 (2022).

[51] D. Cogan, Z.-E. Su, O. Kenneth, and D. Gershoni, A deterministic source of indistinguishable photons in a cluster state, arXiv:2110.05908.

[52] we identify the H, B, and R polarizations with $\hat{x}$, $\hat{y}$, and $\hat{z}$, respectively.

[53] The error estimate Δ_{psv} appearing in $\tilde{F}_0$ is constructed in the standard way from the error estimates ΔR and ΔS. The error Δs is now taken care of by the second term (and Δp is negligible anyway).

[54] M. Paris and J. Řeháček, eds. *Quantum State Estimation* (Springer, Berlin, 2004).

[55] M. Ziman, M. Plesch, V. Bužek, and P. Štelmachovič, Process reconstruction: From unphysical to physical maps via maximum likelihood, Phys. Rev. A **72,** 022106 (2005).

[56] It is convenient to extend F to arbitrary matrices by defining $F(A) = F(\frac{1}{2}(A + A^{\dagger}))$.

[57] Euclidean gradient descent fails even if one includes a similar improvement in it.

[58] The need for the Lagrange multiplier is a cost that we pay for using a nonflat metric. In a flat metric, the constraints may be solved trivially.